Meas. Sci. Technol. **19** (2008) 045501 (11pp) doi:10.1088/0957-0233/19/4/045501

A magnetic induction tomography system for samples with conductivities below 10 S m^{-1}

S Watson[1], R J Williams[1], W Gough[2] and H Griffiths[3]

[1] Faculty of Advanced Technology, University of Glamorgan, Pontypridd CF37 1DL, UK
[2] Department of Physics and Astronomy, Cardiff University, Cardiff CF24 3AA, UK
[3] Department of Medical Physics & Clinical Engineering, Singleton Hospital, Swansea SA2 8QA, UK

Received 23 August 2007, in final form 12 December 2007
Published 7 February 2008
Online at stacks.iop.org/MST/19/045501

Abstract
A 16-channel magnetic induction tomography (MIT) system has been constructed for imaging samples with low conductivities (<10 S m^{-1}) such as biological tissues or ionized water in pipelines. The system has a fixed operating frequency of 10 MHz and employs heterodyne downconversion of the received signals, to 10 kHz, to reduce phase instabilities during signal distribution and processing. The real and imaginary components of the received signal, relative to a synchronous reference, are measured using a digital lock-in amplifier. Images are reconstructed using a linearized reconstruction method based on inversion of a sensitivity matrix with Tikhonov regularization. System performance measurements and images of a pipeline phantom and a human leg *in vivo* are presented. The average phase precision of the MIT system is 17 millidegrees.

Keywords: bioimpedance, tomography, magnetic induction, MIT, EMT, sub-sea oil production

1. Introduction

Magnetic induction tomography (MIT, also known as electromagnetic induction tomography (EMT)) is a technique for imaging the passive electromagnetic properties of an object. MIT applies a magnetic field from a current-carrying coil to induce eddy currents in the object which are then sensed by an array of other coils. Compared with the related technique, electrical impedance tomography (EIT), MIT has the advantage that it does not require direct contact with the object but operates through an air gap. Another technique, electrical capacitance tomography (ECT), can operate through an air gap but is unsuitable for conductive materials because the air layer dominates the response. The contactless nature of MIT means that errors due to electrode contact impedances are avoided completely and that the positions of the coils are known and remain fixed, an advantage for image reconstruction. In principle, more coils could be added to an MIT array to increase spatial resolution without any loss of practicality. Alternatively, the array can be translated along an object to provide cross-sectional images at different levels [1]. Magnetic coupling allows eddy currents easily to be induced in samples surrounded by high-resistivity barriers, for example in the brain, through the skull, and into pipes or vessels constructed from non-conducting materials.

Initial progress in MIT was most rapid in imaging metals because their high conductivities produce large eddy-current signals and the metals industry is very familiar with inductive sensors; from this a range of industrial applications is now emerging [2–4]. The development of MIT for biomedical use has been much more difficult because the electrical conductivities of biological tissues (0.02–2 S m^{-1}) are many orders of magnitude lower than those of metals and give much weaker signals. Nevertheless, our work and that of others has shown that the technological difficulties are being overcome, that the signals are measurable and that images can be reconstructed [2–10]. Proposed applications include imaging cerebral stroke, body composition, wound healing and bioelectrical spectroscopy. Industrial applications in imaging conductivities similar to those of biological tissues have also been suggested, such as the imaging of ionized water in pipelines and separators and imaging foodstuffs [2–4]. All these applications, biomedical and industrial, where the conductivity is less than about 10 S m^{-1}, can conveniently be termed 'low-conductivity' applications and pose research

questions of a generic nature especially with regard to signal capture and image reconstruction.

In this paper, we describe the design and performance of a 10 MHz, 16-channel, MIT system and show preliminary imaging experiments on a human leg *in vivo*.

In addition, we address what is potentially a new industrial application of MIT in off-shore oil production, where knowledge of the seawater fraction ('water cut') in multiphase flow in pipelines and separators is important for controlling productivity. Various commercial sensors are available employing capacitance, microwaves, ultrasound or γ-rays, but their accuracy has been limited by factors such as scaling of the pipes, a limited range and the gas content of the mixture. Eddy-current techniques could provide a complementary method because they would be sensitive only to the conductive component of the mixture, i.e. the process water, which has a typical conductivity of 5 S m^{-1}. Furthermore, the use of several coils and possibly multiple frequencies would enable the conductivity of the process water to be determined. Albrechtsen *et al* [11] demonstrated an experimental system using a single excitation coil with phantoms simulating different flow regimes. With non-cylindrically-symmetrical flow (e.g. stratified), the derived water fraction depended strongly on the position of the coil relative to the water/oil interface; the authors concluded that to overcome this problem, a tomographic system should be developed. More recent work by another Norwegian research group using a single-channel inductive system has also concluded that the work should be extended to tomography [12].

In this paper, we report what we believe to be the first such measurements and describe MIT imaging of a phantom simulating multiphase flow in an oil pipeline.

2. The MIT signal

There are two contributions to the signal detected by the sensing coil in MIT. The first is directly induced by the field from the excitation coil (the primary signal, V). The second is from the eddy currents induced in the material which in turn produce their own magnetic field which induces a further emf in the detector coil (the secondary signal, ΔV). For a sinusoidally-time-varying excitation at angular frequency ω, the skin depth of the electromagnetic field in the material (strictly for a plane wave) is given by $\delta = (2/\omega\mu_0\mu_r\sigma)^{1/2}$, where σ and μ_r are the electrical conductivity and relative permeability of the sample and μ_0 is the permeability of free space. If δ is large compared with the thickness of the sample, which will often be so for a segment of the human body,

$$\frac{\Delta V}{V} = Q\omega\mu_0\left[\omega\varepsilon_0\left(\varepsilon_r - 1\right) - \mathrm{i}\sigma\right] + R(\mu_r - 1), \qquad (1)$$

where ε_r is the relative permeability of the sample, ε_0 is the permittivity of free space, and Q and R are geometrical constants [13]. So, the conduction currents induced in the sample give rise to a component of ΔV which is proportional to frequency and conductivity and is imaginary and negative, meaning that it lags the primary signal by 90°. Displacement currents cause a real (in-phase) component proportional to the square of the frequency. A non-unity relative permeability also gives rise to a real component, but with a value independent of frequency. For the experiments described in this paper, it will be assumed that $\mu_r = 1$.

3. System design

3.1. Overview

The MIT system comprises four subsystems:

- the front end, consisting of the chassis/screen, the 16 coil modules and the transmitter (excitation) and receiver (detection) circuitry;
- the signal-distribution and control system;
- the measurement system;
- the image-reconstruction system comprising the data storage, forward-modelling software, image-reconstruction algorithm and image-visualization software.

The operating principle is as follows. One of the 16 channels is selected as the active transmitter channel, and the oscillator and power amplifier on the transmitter circuit board are enabled. The transmitter circuits of all other 15 channels are disabled. The receiver circuits of each of these 15 channels are then sequentially enabled.

The signals are de-multiplexed to the measurement system which measures each signal as a complex number, i.e. with in-phase and in-quadrature (real and imaginary) components relative to a synchronous reference waveform. One frame of data consists of 240 such measurements covering all the transmitter/receiver coil combinations (16 × 15). For imaging, two frames are measured, a data frame with a sample placed within the detector space and the other, a reference frame for an empty detector space or some other reference condition. An image of the conductivity or permittivity distribution of the sample is then reconstructed.

Details of the subsystems are given in the following sections.

3.2. Chassis/screen

The MIT system front end consists of a cylindrical electromagnetic screen of aluminium (350 mm in diameter, 250 mm in height) within which are attached 16 coil modules (see figure 1). Sixteen corresponding transmitter and receiver circuit modules are housed in metal enclosures attached to the outside of the screen. In concept, this construction is very similar to that of the Moscow MIT system [5] but the detailed design is original to our research group.

The electromagnetic screen (i) provides a rigid chassis to support the coils, (ii) reduces interference from external electromagnetic fields, (iii) confines the excitation field within the imaging volume, thereby removing the potential for interference by external conductive or magnetic objects and (iv) acts as a ground plane that helps to reduce undesirable electric-field (capacitive) coupling between the excitation and detection coils. In a recent paper, we have shown that the capacitive coupling in this system is very small indeed [13].

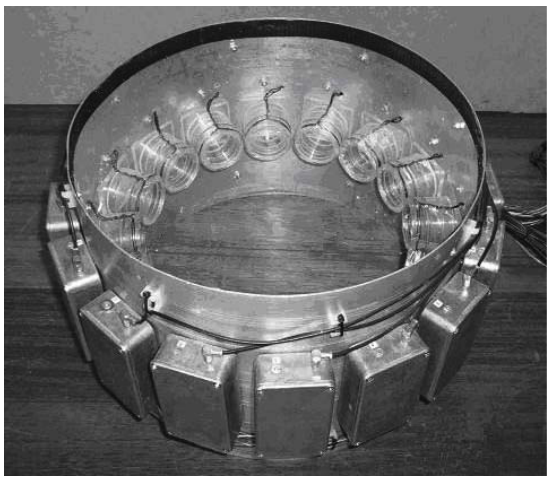

Figure 1. The MIT front end showing the coils fixed inside the electromagnetic screen.

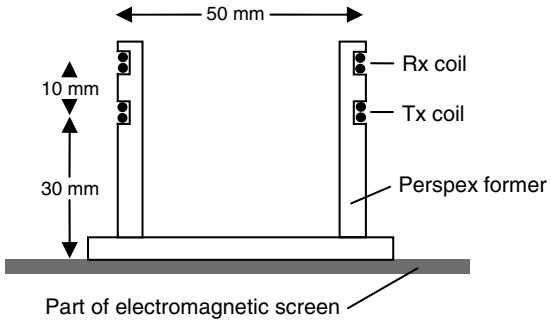

Figure 2. Detail of individual coil module. Rx = receiver, Tx = transmitter.

3.3. Coils

The constructional details of the coil modules are shown in figure 2. The transmitter coils consist of two turns of 0.6 mm diameter, PVC-insulated, solid, copper wire; this number of turns was found to provide the best combination of magnetic field strength ($\propto$ current $\times$ number of turns) and load impedance at 10 MHz. The receiver coils also had two turns which set the self-resonance frequency above 50 MHz. This reduced the potential for phase instability which was found to increase when operating near the resonant frequency. It also avoided resonance at harmonics of the operating frequency; with four turns, for instance, the coil exhibited resonances at approximately 30 MHz and 50 MHz, causing significant distortion of the 10 MHz signals.

3.4. Excitation circuitry

The design of the transmitter module is shown in figure 3. The excitation signal source is a 10 MHz, temperature-compensated, crystal-oscillator module which is enabled when the channel is to be used as the transmitter. When the oscillator is disabled, its power supply is also disconnected by means of a relay. The output of the oscillator is passed to a buffer and then to a coil-driver amplifier with a balanced output which provides

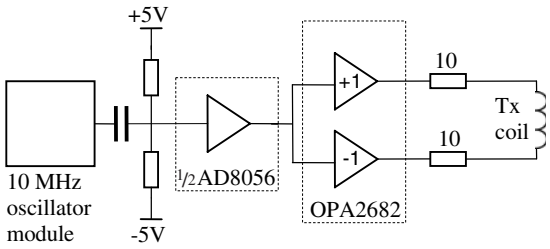

Figure 3. Transmitter module design.

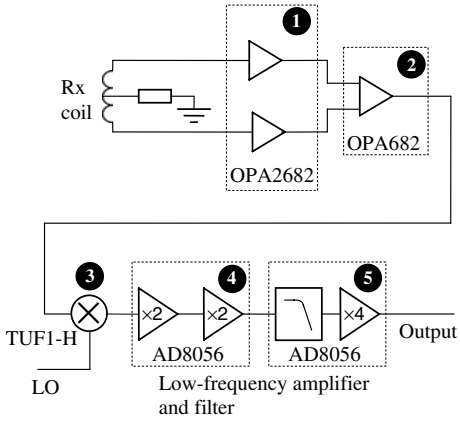

Figure 4. Receiver module design. The numbers, 1–5, shown against the components relate to measurements presented later in section 5.2. LO = input from local oscillator.

an excitation current of approximately 100 mA r.m.s. The output amplifiers (OPA2682) have a disable function which places their outputs into a high-impedance state. This function was used to minimize the loading of the transmitter coil when not in use and hence minimize its interaction with any of the other coils by inductive coupling. The specifications of the OPA2682, for the disabled state, quote an impedance from its output to ground of 800 Ω in parallel with 4 pF for the inverting configuration and 1 MΩ in parallel with 4 pF for the non-inverting. Including also the two 10 Ω resistors in series with the amplifier outputs (figure 3), this means that when not in use, the coil will be shunted by an impedance of (805–4133i) Ω.

3.5. Detection circuitry

The receiver module circuitry (figure 4) consists of a wideband differential amplifier with unity gain, formed from two devices (OPA2682 and OPA682). This allows conversion of the received signal from balanced to unbalanced. The balanced input stage helps to provide further rejection of unwanted interference due to capacitive coupling with the transmitter coil [4]. The signal is passed to a mixer (Minicircuits TUF1-H) where it is mixed with a 9.99 MHz waveform from a local oscillator, thus downconverting it to 10 kHz. The 9.99 MHz waveform is derived from a single, low-phase-noise generator (Marconi 2022C) and is distributed to each receiver channel via a power amplifier (AD815) and a 1:16 resistive power

splitter. The mixer output then undergoes low-pass filtering (single pole $f_t = 30$ kHz) to remove the sum frequency, and three stages of amplification in a circuit which exhibited a low phase drift and phase skew [14].

3.6. Signal distribution and measurement

The downconverted signals from the receivers are distributed to two analogue multiplexers (ADG406), one of which selects the received signal, and the other the reference signal (2.1 V r.m.s.) derived from the receiver coil of the channel active as the transmitter. It is assumed here that the signal derived from the receiver coil on the same coil former as the active transmitter coil can be employed as a reference since, due to its proximity to the transmitter coil, it will be sensitive almost entirely to the primary field and will be hardly affected by a sample placed within the array.

The measurement system is a digital lock-in amplifier (Stanford Research Systems 830) controlled by a PC via a GPIB interface. The lock-in amplifier operates as a vector voltmeter, providing the real and imaginary components of the received signal relative to the phase of its internal reference signal.

Once the reference frame (empty detector space) and data frame (sample in place) have been acquired as sets of complex numbers, the differences between the data and reference measurements, ΔV, are divided by the reference measurements, V, to form the quantities $\mathrm{Re}(\Delta V/V)$ and $\mathrm{Im}(\Delta V/V)$, compatible with equation (1). Since these quantities contain ratios of signals, the influence of any variations in the receiver gains between channels and over time is reduced. The total time taken to acquire one frame of data (240 complex numbers) is 90 s.

4. Forward modelling and image reconstruction

Images of conductivity were reconstructed from the measured values of $\mathrm{Im}(\Delta V/V)$. First, the sensitivity matrix, $\mathbf{S}$, was computed using a finite-difference forward model of the system [15]. The volume was divided into cuboidal voxels and $\mathbf{S}$ was computed using two different methods. For perturbations in conductivity relative to empty space, $\mathbf{S}$ was computed by setting the conductivity of each voxel in turn to 1 S m^{-1}. For perturbations relative to a conductive background, $\mathbf{S}$ was computed using the reciprocity principle [16]. For each transmitter/receiver coil combination, the sensitivity S_i of voxel i, with conductivity σ_i, is given by

$$S_i = \frac{\mathbf{J}_{\mathrm{T}i} \cdot \mathbf{J}_{\mathrm{R}i}}{\sigma_i}, \tag{2}$$

where $\mathbf{J}_{\mathrm{T}i}$ is the eddy current density induced within voxel i by the transmitter coil, and $\mathbf{J}_{\mathrm{R}i}$ is the eddy current density which would be induced by the receiver coil if it were employed as the transmitter. $\mathbf{S}$ then has as many rows as there are voxels in the volume and as many columns as there are coil combinations.

Expressing the forward problem as

$$\mathbf{S}\boldsymbol{\sigma} = \mathbf{b}, \tag{3}$$

where $\boldsymbol{\sigma}$ is the unknown conductivity distribution and $\mathbf{b}$ is the measurement vector, the conductivity distribution, $\boldsymbol{\sigma}_\lambda$, reconstructed using Tikhonov regularization, is given by

$$\boldsymbol{\sigma}_\lambda = \min_{\boldsymbol{\sigma}} \left\{ \|\mathbf{S}\boldsymbol{\sigma} - \mathbf{b}\|_2^2 + \lambda^2 \|\mathbf{L}(\boldsymbol{\sigma} - \boldsymbol{\sigma}_0)\|_2^2 \right\}, \tag{4}$$

where λ is the regularization parameter, $\mathbf{L}$ is the regularization matrix and $\boldsymbol{\sigma}_0$ is an *a priori* estimate of $\boldsymbol{\sigma}$. For all the reconstructions presented in this study, $\mathbf{L}$ was set to the identity matrix and no *a priori* information was incorporated, i.e. $\boldsymbol{\sigma}_0 = \mathbf{0}$. Images were reconstructed using a MATLAB regularization toolbox [17]. λ was selected by a subjective assessment of the smallest value, consequently giving the highest spatial resolution, which did not introduce significant noise artefacts.

5. Measurements

5.1. Noise and drift

To determine the noise of the system, a reference frame was collected. A second 'data' frame was then collected after an interval of 10 s; both frames were collected with no sample present in the array. $\mathrm{Im}(\Delta V/V)$ was computed for each transmitter/receiver combination, as described in section 3.6. This was repeated ten times and the average noise for each channel was calculated as the standard deviation of the ten measurements. The system's average noise was calculated by averaging over all 240 channel combinations.

To determine the system's drift, 30 frames were collected spaced at 10 s intervals, giving a total measurement time of 48 min. The drift was calculated by taking the difference between the maximum and minimum values of $\mathrm{Im}(\Delta V/V)$ over the 30 measurements for each transmitter/receiver combination. The system's average drift was then defined as the average over all channel combinations. The maximum drift was defined as the figure obtained for the channel combination showing the highest drift figure.

5.2. Temperature sensitivity of receiver components

As temperature changes are a common cause of drift in electronic systems, an investigation was performed to determine the sensitivity of the phase of the signal to changes in temperature of the active devices in the receiver circuit. Heat-sink compound (HTCP, Electrolube, Berkshire, UK) was applied to the tops of five components of the receiver circuit—the first and second stages of the RF input amplifier, the mixer, the low-frequency amplifier and the filter and amplifier section (labelled 1–5 in figure 4).

Measurements of the receiver output were made at the rate of 2 s^{-1} for a period of 10 min during which time a broad-tipped soldering iron was held against each device in turn for 5 s, via the heat-sink compound. The sequence of measurements was repeated twice. A further three sequences were acquired, but this time with the soldering iron applied to the corresponding components in the receiver circuit of the reference channel.

A second experiment was then performed in which separate circuit boards for the individual devices were constructed, allowing each to be placed in a temperature-controlled oven. The change in phase of the signal in response

Figure 5. The MIT system imaging a simulated oil/gas/water mixture in a cylindrical pipe phantom.

Table 1. Details of the four subjects imaged.

Subject	Height (m)	Weight (kg)	Mean thigh diameter (mm)
1	1.80	88	143
2	1.66	67	146
3	1.82	85	152
4	1.88	94	156

to temperatures in the range 30–60 °C was recorded. The measurements were carried out four times for each device.

5.3. Imaging-simulated multiphase flow

A cylindrical plastic tube (diameter 200 mm, length 500 mm) was positioned coaxially through the coil array. It was then filled to different levels with saline, 5 S m^{-1} in conductivity, to simulate stratified flow, and a data set was acquired for each level. It was assumed that the air in the pipe represented the oil and gas in a real pipeline as oil is non-conductive and has a low relative permittivity ($\varepsilon_r < 5$) compared with that of water. The tube was supported by a horizontal platform along which it could be slid out of the array for the reference frame of data to be acquired (see figure 5).

5.4. In vivo imaging

In a second imaging experiment, the purpose was to obtain *in vivo* images of the human thigh. Four volunteers from university staff were recruited (table 1). The MIT array was positioned again with its axis horizontal to enable the leg of a supine subject to be imaged. First, a reference set of data was acquired with the array empty. The leg was then inserted through the array such that the coils were approximately midway between the knee and the groin. The mean diameter of the thigh at this level was measured and also its vertical position within the coil array. An MIT data set was then acquired.

As a calibration, a plastic cylinder of saline solution (diameter 150 mm, length 200 mm) was positioned at the same vertical position in which the leg had been. MIT measurements were obtained for different values of the conductivity of the solution.

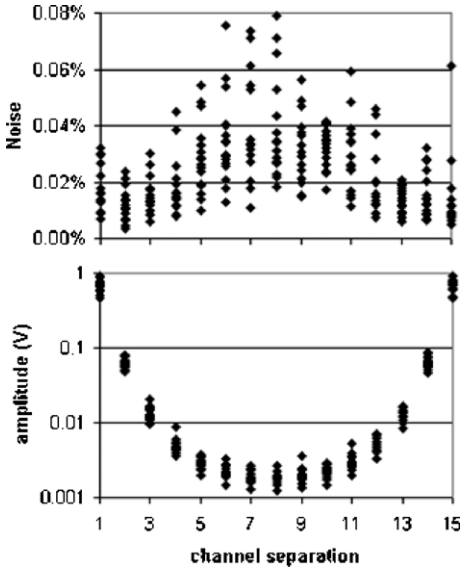

Figure 6. Upper graph: average noise in Im($\Delta V/V$) for the 240 different channel combinations. Lower graph: the primary signal, V, in Volts r.m.s. at the receiver output (see figure 4). The channel separation is the separation of the receiver from the transmitter in a clockwise sense (in units of 22.5°).

5.5. Simulated femur

As a comparison with the thigh measurements, a plastic rod (diameter 36 mm) was immersed in the solution to simulate the femur. The rod was positioned parallel to the axis of the cylinder, with its own axis displaced from that of the cylinder by half of the radius of the cylinder, roughly to represent the anatomical position of the femur in the leg. Further MIT images were obtained.

6. Results

6.1. Noise and drift

The average noise measured for the different channel combinations is shown in figure 6 (see section 5.1). Here, the value of the standard deviation of Im($\Delta V/V$) has been multiplied by 100 so that the noise is expressed as a percentage of the primary signal, V. The average noise for each channel combination varied from 0.005% to 0.08%, the larger values tending to be when the distance between the excitation and detection coil was greatest, since the primary signal was least in these positions. The percentage noise averaged across all channel combinations was 0.03%, corresponding to a phase noise figure of 17 millidegrees. The large scatter in the results for a given channel separation is likely to be due to the fact that some drifting was occurring during the measurement sequence, which lasted 190 s (two frames with a 10 s gap).

The average drift in the received signal, measured as described in section 5.1, was 0.17% and 0.23% for the real

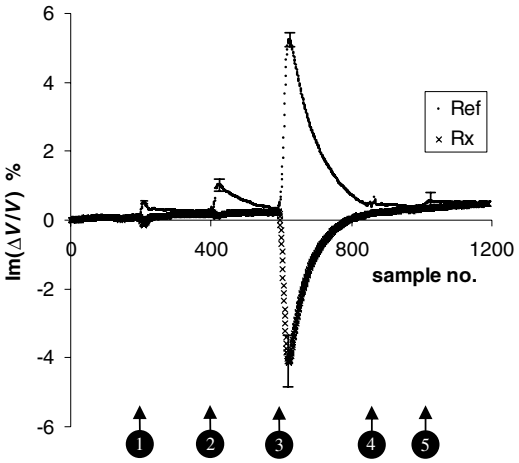

Figure 7. Change in Im($\Delta V/V$) over a 10 min period during which the active devices in the receiver module were heated in turn, at times indicated by the numbered markers (see also figure 4). Two curves are shown, one of measurements when the components of the receiver module of the receiver channel were heated (Rx) and the other when the corresponding components in the receiver module of the reference channel were heated (Ref). Each curve is the mean of three measurements; representative error bars are shown, equal to ± 1 standard error.

Table 2. Temperature coefficients of phase change (mean ± 1 standard error) measured by heating the devices in an oven.

Component	Temperature coefficient of phase change (millidegrees $^{\circ}C^{-1}$)
OPA2682	11 ± 0.5
OPA682	11 ± 0.5
TUF-1H	94 ± 5
AD8056	7 ± 1

and imaginary components, respectively, while the maximum drift was 1.5% and 1.3% (860 and 745 millidegrees). These measurements demonstrate that the drift was very large compared with the random noise and a significant source of error in this MIT system.

6.2. Temperature sensitivity of receiver components

The results of heating of the individual active components in the receiver circuit are shown in figure 7. A change in Im($\Delta V/V$) was observed when each of the five devices in the receiver circuit of the receiver channel was heated with the soldering iron. By far the most sensitive device was component 3, the TUF1-H mixer, which showed a change of -4.2% (2400 millidegrees in phase). When the corresponding components in the receiver circuit of the reference channel were heated, very similar changes were observed but, as expected, with the opposite sign.

For the second experiment, in which the devices were placed separately in an oven, the results are shown in table 2. The observation from the first experiment was confirmed: that the TUF1-H mixer was by far the most temperature-sensitive component, having a temperature coefficient more than eight times greater than that of any of the other devices.

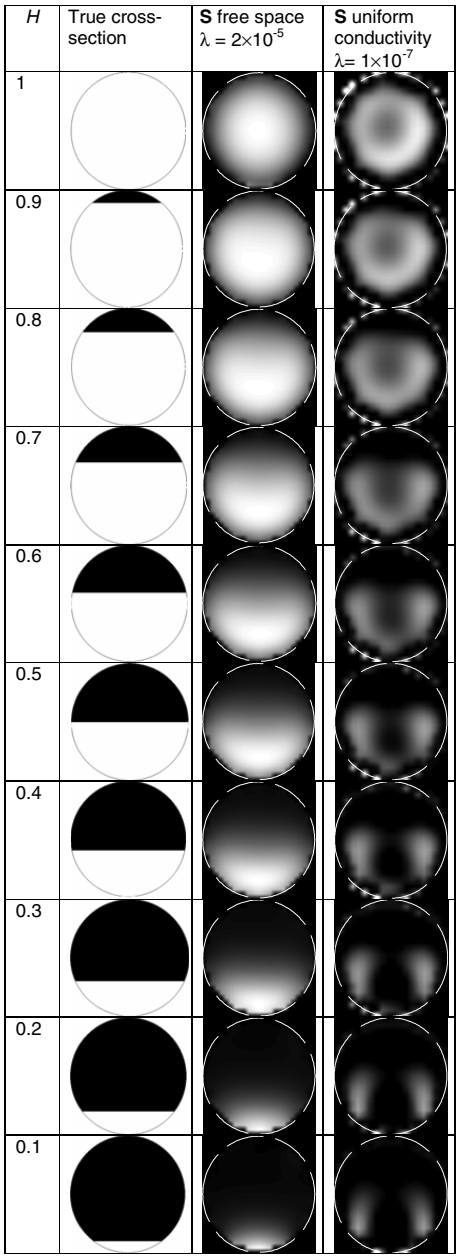

Figure 8. MIT images of a simulated oil/gas/seawater mixture in a pipeline for different fractional depths, H, of saline solution. The second column indicates the true cross-section of the saline in the pipe (white area). The third and fourth columns contain images reconstructed with the two different sensitivity matrices; in each case, the regularization parameter, λ, is given. The white circle indicates the position of the pipe wall.

6.3. Imaging-simulated multiphase flow

Figure 8 shows the images obtained for different volume fractions of the saline solution in the cylindrical phantom simulating stratified flow of an oil/gas/seawater mixture in a pipeline. The images were reconstructed from the measured values of Im($\Delta V/V$), using a sensitivity matrix computed by dividing the cylinder into $20 \times 20 \times 50$ cubic voxels, of side-length 10 mm. The first set of images (column 3)

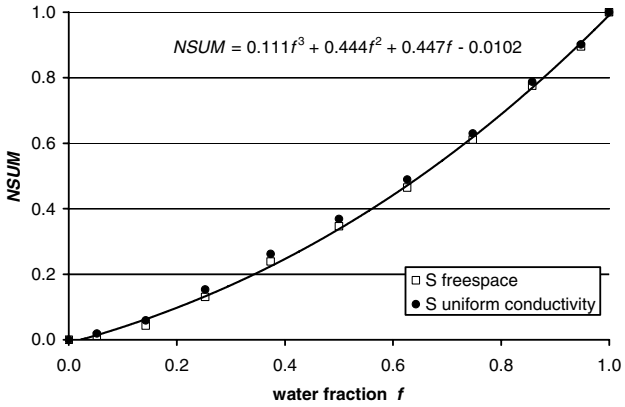

Figure 9. Sum of the image values, *NSUM*, normalized to the figure for a full pipe, versus water fraction, for the two series of images in figure 8. A third-order polynomial is fitted to the points for the images reconstructed with a free-space sensitivity matrix (equation given).

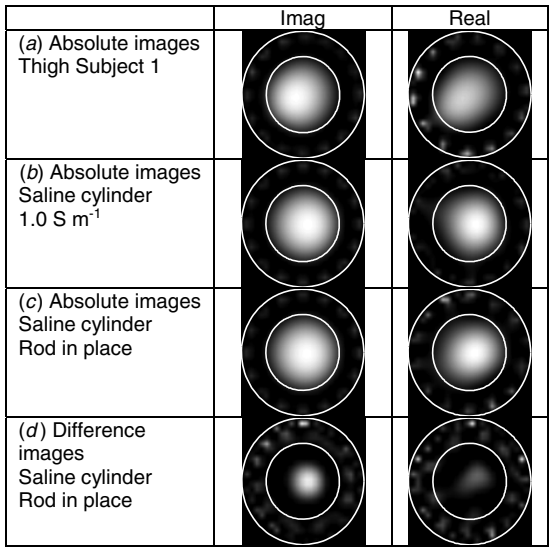

Figure 10. Images reconstructed from the real and imaginary parts of the data for (*a*) human subject 1 and (*b*)–(*d*) the saline phantom. The inner white circle is the region of interest applied for summing the image values. The regularization factor, λ, was 2×10^{-6} for rows (*a*)–(*c*) and 1×10^{-7} for row (*d*). The sign of the image was changed for images (*a*)–(*c*) in the left-hand column, so that in all cases, the main image feature appeared as a bright area. All images were normalized to the maximum image value (even if located in an artefact).

were reconstructed using a sensitivity matrix computed for free space as described in section 4. The second set of images (column 4) were reconstructed using a sensitivity matrix computed for a uniform conductivity within the pipe, using the reciprocity principle (equation (2)). In both cases, the reference frame of data was measured with the cylinder removed from the MIT array (i.e. for free space).

The main image feature resulting from the conductive saline solution (bright area) is negative. Any positive image values occurring near the edge of the images were set to zero.

The images reconstructed with the sensitivity matrix relating to free space give a better impression of the cross-section of the simulated seawater in the pipe. The images reconstructed for the conductive background show the main area of conductance compressed inwards from the wall and a void at the centre; they also show artefacts at the pipe wall.

In order to generate a 'response curve', the image values were summed over the whole image and normalized to the figure obtained for a full pipe ($H = 1$). This sum is plotted in figure 9 against the water fraction, f, calculated from the value of H, which can readily be shown to be related to f by the formula

$$f = \frac{1}{\pi}[\cos^{-1}(1-2H) - 2(1-2H)\sqrt{H-H^2}]. \qquad (5)$$

Although the two sets of images are different in appearance, the normalized responses are very similar and closely represented by a third-order polynomial as shown.

6.4. *In vivo imaging*

Figure 10(*a*) shows typical images obtained from the thigh of one of the four subjects. These are absolute images, reconstructed from the real and the imaginary parts of the measurements, referenced to free space, and using a sensitivity matrix computed for free space. From equation (1), it is assumed that the image obtained from the imaginary parts represents the conductivity of the thigh and the image from the real parts, its permittivity. Clearly, the images do not have sufficient spatial resolution to detect any internal anatomical structure.

A cylindrical saline phantom of varying conductivity was used as a calibration, allowing the equivalent uniform conductivity and relative permittivity of the thigh to be calculated. Figure 10(*b*) shows the images obtained for one value of the conductivity of the phantom (1.0 S m^{-1}). A circular region of interest was applied to the images to include the image of the phantom but to exclude any noise and edge artefacts in the rest of the image. The sum of the image values within the region of interest was computed: this is termed SUM_{Real} and SUM_{Imag} for the images reconstructed from the real and imaginary parts of the data, $\mathrm{Re}(\Delta V/V)$ and $\mathrm{Im}(\Delta V/V)$, respectively. The two quantities are plotted against saline conductivity in figure 11.

SUM_{Imag} is negative and proportional to conductivity, in close agreement with the theoretical equation (equation (1)). The straight line fitted to the values of SUM_{Imag} was now used as a calibration line (see figure 11). On the images of the thigh, a similar region of interest was applied (figure 10(*a*)). From the value of SUM_{Imag} measured, the equivalent uniform conductivity of the thigh was calculated from the equation of the line and is given in table 3. For the four subjects, the values lie between 0.27 S m^{-1} and 0.50 S m^{-1} and are within the published range for fat and muscle at 10 MHz, the main constituents of the thigh (fat 0.03 S m^{-1}, muscle 0.67 S m^{-1} [18]).

For calculating the equivalent uniform relative permittivity of the thigh, equation (6) was used; this is an adaptation of the equation derived from equation (1) by

Table 3. The sums of the image values from the images of the thighs of the four human subjects. Estimates of the average conductivity and relative permittivity of the thigh are shown. BMI is the body mass index, = weight/(height)^2, calculated from the anthropometric data given in table 1.

Subject	BMI (kg m^{-2})	SUM_{Imag}	SUM_{Real}	Equivalent uniform conductivity of thigh (S m^{-1})	Equivalent uniform relative permittivity of thigh
1	27.2	−692	55.8	0.27	40
2	24.3	−837	77.7	0.33	55
3	25.7	−1140	94.8	0.44	67
4	26.5	−1290	122	0.50	86

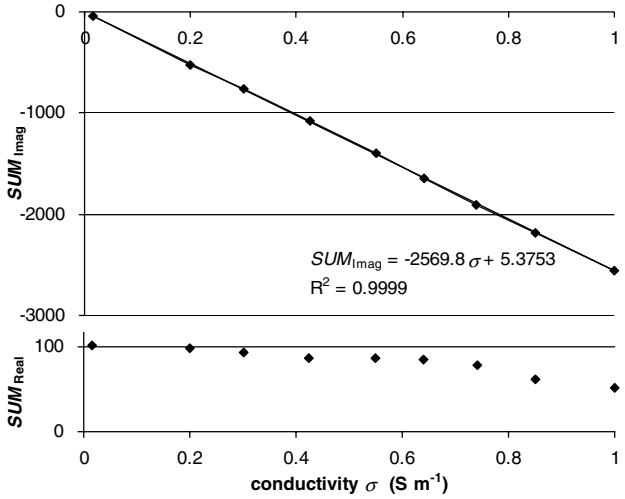

Figure 11. Plots of SUM_{Imag} and SUM_{Real} against the conductivity of the saline cylinder. The straight line fitted to SUM_{Imag} is drawn and its equation and coefficient of determination, R^2, given. The standard deviation of the measurements was 10.

Griffiths *et al* [13], but now using the values of SUM_{Real} and SUM_{Imag} obtained from the images, instead of the real and imaginary parts of the measurements themselves. The derivative in the denominator is simply the gradient of the calibration line used above (−2570 S^{-1} m). The derived values of the equivalent uniform relative permittivity of the thighs of the four subjects are given in table 3 and lie between 40 and 86. Again, they are within the range for fat and muscle at 10 MHz (fat 15, muscle 135–153 [18]). Neither the equivalent uniform conductivity nor the relative permittivity appears to be correlated with the body mass index of the subjects (table 3).

$$\varepsilon_{\mathrm{r}} = \frac{-SUM_{\mathrm{Real}}}{\omega\varepsilon_0 \frac{\partial}{\partial\sigma}(SUM_{\mathrm{Imag}})} + 1. \qquad (6)$$

Equation (1) predicts that $\mathrm{Re}(\Delta V/V)$, and hence SUM_{Real}, should be proportional to the relative permittivity of the target. The relative permittivity of saline solution falls slightly with increasing salinity; Hilland [19] reported a drop of 1–3% as the conductivity increased from 0 S m^{-1} to 1 S m^{-1}. In the results presented in figure 11, SUM_{Real} fell by a much larger amount, by almost 50% over the same conductivity range; this cannot be explained by a change in the relative permittivity of the saline solution. Griffiths *et al* [13] observed a similar behaviour in measurements made with a single channel and demonstrated that it was due to the skin effect. They found that although $\mathrm{Im}(\Delta V/V)$ closely maintained its proportionality to conductivity (as does SUM_{Imag} in the present study), $\mathrm{Re}(\Delta V/V)$ departed from equation (1) even when the skin depth was greater than the dimensions of the phantom used. This means that the value of ε_{r} obtained using equation (6) will be accurate only at very low conductivities and will be underestimated at higher conductivities.

For the lowest conductivity of the saline phantom (0.016 S m^{-1}), the value of SUM_{Real} was 102 (see figure 11) and equation (6) leads to a value, $\varepsilon_{\mathrm{r}} = 72$. This is comparable with the known value for water (80 at 20 °C) within the measurement noise. At a conductivity of 1.0 S m^{-1}, SUM_{Real} had fallen to 52, giving $\varepsilon_{\mathrm{r}} = 37$, even though the diameter of the phantom (150 mm) was still only equal to 0.94δ.

The extent of the error in the measurements of the relative permittivity for the thigh, due to the skin effect, can be judged from the measurements of SUM_{Real} for the phantom, given in figure 11. For the range of conductivities estimated for the thigh (0.27–0.50 S m^{-1}, see table 3), the value of SUM_{Real} for the phantom has dropped by 5–10% relative to its value at very low conductivities. This implies that the derived values of the relative permittivity of the thigh should be increased by 5–10%. With this adjustment, they still lie within the known range for fat and muscle.

6.5. *Simulated femur*

Imaging the saline phantom containing a plastic rod (section 5.5) was performed in order to investigate the fact that even a high-contrast structure such as the femur could not be distinguished on the images of the thigh (figure 10(*a*)). Figure 10(*c*) shows the absolute images of the phantom obtained. They do not reveal the rod.

Figure 10(*d*) shows difference images reconstructed using a frame of data measured for the uniform saline cylinder as a reference rather than a frame obtained for empty space. The rod is now clearly visible, demonstrating that the information on this internal structure is indeed contained within the measurements, well above the noise level. It appears, therefore, that the inability of the absolute images to show the plastic rod (figure 10(*c*)) or the femur (figure 10(*a*)) is due to the inadequacy of the image reconstruction algorithm and not the performance of the MIT data-collection system.

7. Conclusions

A 10 MHz experimental MIT system has been developed as a first stage towards a non-contacting biomedical imaging

system and an industrial imaging system for targets with conductivities of less than about 10 S m^{-1} that need to be viewed through an air gap or some other insulating barrier.

In a new application of MIT, a phantom simulating stratified flow of an oil/gas/seawater mixture in a pipeline was used to demonstrate imaging of the water component. The images allowed the cross-section of the water to be visualized. It was found that the response curve of the normalized integrated image value plotted against water fraction was insensitive to the sensitivity matrix used for the image reconstruction. Further development of the reconstruction algorithm must now take place and the system must be tested with other flow regimes, e.g. bubble and annular (see [11]). The reference was obtained by acquiring a frame of data with the simulated pipeline removed from the MIT array. This would not be feasible in an industrial context as the MIT array would need to be permanently attached around the pipeline. Other methods of referencing the image must therefore be developed, e.g. the use of multiple frequencies. The present imaging system is very slow (one frame per 90 s) and it is likely that much higher frame rates will be required for industrial use. However, the high conductivity of the process water ($\approx$5 S m^{-1}) relative to targets of interest in other applications (e.g. biological tissues), should mean that a good SNR can be achieved with a much shorter integrating time and a consequent increase in speed.

Imaging of the thigh, *in vivo*, in a group of volunteers was demonstrated. No internal anatomical structure was discernable on the absolute images (referenced to empty space), but a method for estimating the equivalent uniform conductivity and relative permittivity of the limb segment was demonstrated. A phantom experiment, using a saline cylinder representing the thigh with an insulating rod simulating the femur, similarly showed that the rod could not be distinguished on absolute images. However, difference images were able clearly to show the rod. This indicates that the spatial resolution and contrast was not limited by the noise in the measurement system but by the image reconstruction algorithm. The spatial resolution could be increased by using a smaller coil array so that the target occupied a larger proportion of the imaging space, but improvement of the image reconstruction algorithm is probably the main area that needs development. The ability to perform difference imaging *in vivo* must also be explored and may allow better distinction of the internal structures. Difference imaging was not possible in this *in-vivo* experiment (as it was not possible to remove the femur and then replace it!) but frequency-difference imaging in future might provide a suitable method. Time-difference imaging may also be appropriate for some biomedical applications (e.g. imaging regional lung ventilation), and some industrial ones (e.g. monitoring contamination in food products on a production line) but would need a faster imaging system than the present one.

The speed of the system is not limited by the integration time but by a number of other processes within the lock-in amplifier: (i) the time it takes to 'acquire lock', i.e. to measure the signal frequency and synthesize its own internal reference, (ii) the settling time for the filters and (iii) the time taken to make the measurement and transfer it to the PC via the GPIB. The total time taken by these processes is 375 ms. An improved MIT system design would be fully synchronous, with signals derived from a single master oscillator distributed to all transmitter and receiver modules so that phase locking would be needed only at the start of the measurement cycle. Higher-order filters with a shorter settling time and a more efficient data transfer could also shorten the measurement time. A very large improvement, by a factor of 15, could be achieved by using parallel data acquisition rather than the present serial method.

In the reconstruction of images, the choice of the regularization parameter, λ, was subjective, whereas an objective method would have been preferable, e.g. the L-curve or generalized cross-validation (GCV) methods. We and others have previously used the L-curve method successfully for reconstructing differential images of low-contrast perturbations relative to a conductive background [20]. For the absolute images reconstructed in this study, the method was found to fail because the curves did not form well-defined 'L' shapes, instead showing multiple, weak maxima of curvature. Similarly, the GCV method did not produce a well-defined minimum and both methods resulted in under-regularized images. Other workers have reported similar difficulties and cited 'geometry noise' as an explanation, i.e. when the model used for computing the sensitivity matrix is too poor a fit to the true measurement system and systematic errors dominate over random measurement noise [21]. An additional difficulty is that, even with accurate geometry, a sensitivity matrix suitable for single-step reconstruction of absolute images is unlikely to exist unless sufficient information is known about the conductivity distribution *a priori*. As far as we are aware, no one has yet demonstrated a successful, general, single-step method for reconstructing absolute images of extended conductivity distributions (although it can be done for well-separated small objects). It is likely that for absolute imaging, iterative, nonlinear reconstruction methods will be necessary and this is the subject of current work in the MIT community.

The short-term random noise level in the data-collection system was measured as 17 millidegrees but the phase drift in the system was much larger, typically 800 millidegrees, and was the main limitation to the accuracy of the measurements. It is likely that the drift was due to temperature variations in the components of the receiver. Two experiments in which the active components in the receiver circuit were heated, directly revealed that the mixer was by far the most sensitive component and should now be the focus of attention for the next design.

In order to reduce the short-term noise level, consideration must also be given to 'backing off' the primary signal, V, at the receiver coil. Watson *et al* [22], using a single channel, achieved a primary-field cancellation factor of 300 over the frequency range 1–10 MHz. They showed further that the noise level fell by a factor of over 40 when the primary field was backed off, suggesting that a significant contribution to the noise was from short-term phase fluctuations between

the primary and reference signals, most probably from phase noise in the reference. Rosell-Ferrer *et al* [10] have achieved primary-field cancellation using planar gradiometers and have successfully constructed a multi-frequency MIT partial array consisting of one excitation coil and 14 receivers. Additional projections were acquired by rotating the target relative to the array, allowing MIT images to be reconstructed. In an accompanying paper, the group demonstrated retrieval of the conductivity spectrum over frequency (100–500 kHz) from the images of a potato immersed in saline solution [23]. Thermal drift was identified as the main source of error in the measurements.

An indication that phase noise in the reference signal was significant in our MIT system is seen from figure 6. The amplitude of the primary signal ranged over nearly three decades between the receivers closest to the transmitter and those furthest away (figure 6, lower curve). The noise in the receiver amplifiers is expected to have a constant level so when expressed as a percentage of the primary signal, V, it will vary by the same factor as V itself. The observed variation was very much less than this and by only a factor of 4 over the range of channel separations (from approximately 1–4%, taking the average for each channel separation: figure 6, upper curve). Another source of noise is the lock-in amplifier which continually synthesizes its internal reference signal from the analogue signal applied to its reference channel. This synthetic reference will have a small and varying phase error relative to the actual reference signal [24]. This will contribute noise to the measurement of ΔV that will be proportional to V. Thus, this component of the noise in $\Delta V/V$ will be independent of V and is the most likely explanation of the much smaller range of values seen in the upper curve of figure 6 than in the lower.

A possible source of systematic error is crosstalk in the multiplexers as they have to handle the complete range of amplitudes of the 10 kHz signals (see section 3.6). The inter-channel isolation was measured to be at least 70 dB between adjacent channels of the multiplexer and 98 dB for channels with the greatest separation. In the least favourable case, the primary signal received in the channel diametrically opposite the excitor will have an amplitude of 1.4 mV (figure 6). The reference will contribute a crosstalk of about 0.03 mV (i.e. 2.1 V reduced by 98 dB), and this is equal to about 2% of the received primary signal. The secondary signals of interest (ΔV) will typically be a few per cent of V or less, so the crosstalk will be significant in comparison. However, if the cross-talk does not vary with time, it will effectively become part of the measured primary signals and will have very little effect on the measured values of $\Delta V/V$. Nevertheless, it is an undesirable contamination of the true signals so should be borne in mind in future system design.

It is likely that the design of the next generation of MIT systems will depend on the particular applications targeted, even within the 'low-conductivity' range (<10 S m^{-1}). These differences could be, for example, in the type of coils used (single coil or gradiometer), the choice of operating frequency and the method of demodulation (vector voltmeter, direct phase measurement or direct digitization of the high-frequency signals). For biological tissue characterization, frequencies below 1 MHz are normally chosen as this is where the β-dispersions of tissues mainly occur and there is best contrast between different tissues. For performing tissue characterization by MIT, the method of Rosell-Ferrer *et al* [10] using gradiometers and multiple frequencies, may prove to be the most effective. For imaging haemorrhagic cerebral stroke, it is interesting to note that even at 10 MHz, the conductivity of blood is still at least three times higher than that of brain tissue [18] so these higher frequencies, with their resulting larger signals, may be suitable. For the new industrial application discussed here, imaging the seawater fraction in an oil pipeline, a frequency of at least 10 MHz with single coils may be optimal, possibly combined with an alternative, faster, method of demodulation such as direct phase measurement [5, 14]. A focus by system designers on specific biomedical and industrial applications is now necessary.

Acknowledgements

This work was supported by the Engineering and Physical Sciences Research Council (grants EP/E009832/1 and EP/E009697/1). The authors thank Mr C Craven for mechanical engineering assistance.

References

[1] Peyton A, Mackin R, Goss D, Wan-Daud W, Crescenzo E, Saunders N and Tapp H 2003 Addressing the difficulties in using inductive methods to evaluating human body composition *Biomét. Hum. Anthropol.* **21** 63–71

[2] Griffiths H 2001 Magnetic induction tomography *Meas. Sci. Technol.* **12** 1126–31

[3] Tapp H S and Peyton A J 2003 A state of the art review of electromagnetic tomography *Proc. 3rd World Congress on Industrial Process Tomography, Banff, Canada* pp 340–6

[4] Griffiths H 2005 Magnetic Induction Tomography *Electrical Impedance Tomography: Methods, History and Applications* ed D S Holder (Bristol: Institute of Physics Publishing) pp 213–38

[5] Korjenevsky A, Cherepenin V and Sapetsky S 2000 Magnetic induction tomography: experimental realization *Physiol. Meas.* **21** 89–94

[6] Korzhenevsky A and Sapetsky S 2001 Visualisation of the internal structure of extended conducting objects by magnetoinduction tomography *Bull. Russian Acad. Sci.: Phys.* **65** 1945–9

[7] Watson S, Morris A, Williams R J, Gough W and Griffiths H 2002 The Cardiff MIT system *Proc. IFMBE:EMBEC02, Vienna, Austria (Dec 4–8)* vol 3 part 1, pp 116–7

[8] Karbeyaz B U and Gencer N G 2003 Electrical conductivity imaging via contactless measurements: an experimental study *IEEE Trans. Med. Imag.* **22** 627–35

[9] Igney C H, Watson S, Williams R J, Griffiths H and Dösse1 O 2005 Design and performance of a planar-array MIT system with normal sensor alignment *Physiol. Meas.* **26** S263–78

[10] Rosell-Ferrer J, Merwa R, Brunner P and Scharfetter H 2006 A multifrequency magnetic induction tomography system using planar gradiometers: data collection and calibration *Physiol. Meas.* **27** S271–80

[11] Albrechtsen R A, Yu Z Z and Peyton A J 1995 Preliminary experiments on the investigation of the inductive technique for measuring water content in multiphase flow *Proc. ECAPT, Bergen* pp 205–13

[12] Hammer E A and Fossdal G 2002 A new water-in-oil monitor based on high frequency magnetic field excitation *Proc. 2nd Int. Symp. on Process Tomography, Wroclaw, Poland (Sept. 11–12)* pp 9–16

[13] Griffiths H, Watson S, Williams R J and Gough W 2007 Residual capacitive coupling and the measurement of permittivity in magnetic induction tomography *Physiol. Meas.* **28** S301–11

[14] Watson S, Williams R J, Griffiths H, Gough W and Morris A 2003 Magnetic induction tomography: phase vs. vector voltmeter measurement techniques *Physiol. Meas.* **24** 555–64

[15] Morris A, Griffiths H and Gough W 2001 A numerical model for magnetic induction tomographic measurements in biological tissues *Physiol. Meas.* **22** 113–9

[16] Geselowitz D 1971 An application of electrocardiographic lead theory to impedance plethysmography *IEEE Trans. Biomed. Eng.* **18** 38–41

[17] Hansen P C 1994 Regularization tools: a Matlab package for analysis and solution of discrete ill-posed problems *Numer. Algorithms* **6** 1–35

[18] Gabriel C, Gabriel S and Corthout E 1996 The dielectric properties of biological tissues: I. Literature survey *Phys. Med. Biol.* **41** 2231–49

[19] Hilland J 1997 Simple sensor system for measuring the dielectric properties of saline solutions *Meas. Sci. Technol.* **8** 901–10

[20] Watson S, Igney C H, Dösse1 O, Williams R J and Griffiths H 2005 A comparison of sensors for minimising the primary signal in planar-array magnetic induction tomography *Physiol. Meas.* **26** S319–31

[21] Johnson P R and Gulrajani R M 2000 Selecting the corner in the L-curve approach to Tikhonov regularisation *IEEE Trans. Biomed. Eng.* **47** 1293–6

[22] Watson S, Williams R J, Griffiths H and Gough W 2004 A primary field compensation scheme for planar array magnetic induction tomography *Physiol. Meas.* **25** 271–9

[23] Brunner P, Merwa R, Missner A, Rosell J, Hollaus K and Scharfetter H 2006 Reconstruction of the shape of the conductivity spectra using differential multi-frequency magnetic induction tomography *Physiol. Meas.* **27** S237–48

[24] Meade M L 1983 *Lock-in Amplifiers: Principles and Applications, IEE Electrical Measurement Series 1* (London: P. Peregrinus) (Chapter 4 'Lock-in amplifier specifications', pp 70–1)